

# Influence of Al and Ca on the Ductility of Mg–Al–Ca Alloys

Wassilios J. Delis,\* Pia C. Huckfeldt, Bengt Hallstedt, Pei-Ling Sun, Dierk Raabe, Sandra Korte-Kerzel, and Stefanie Sandlöbes-Haut

Magnesium and its alloys offer huge potential for lightweight applications. However, many Mg alloys suffer from limited room-temperature formability. It has previously been shown that the addition of aluminium and calcium to Mg can improve ductility. Therefore, in the present work, it is aimed to systematically vary the alloying content of Al and Ca and to study their effects on the slip system activity and crystallographic texture after rolling and recrystallization. In the results, it is shown that all investigated ternary alloys in the range of 1–2 wt% Al and 0.005–0.5 wt% Ca have an increased ductility (in the range of 10–17% increase compared to pure Mg), whereas the binary Mg–Al and Mg–Ca alloys suffer from limited ductility (10% tensile elongation) and strength (175 MPa ultimate tensile strength). Non-basal and especially  $\langle c + a \rangle$ -slip is active in all compositions (in 15–33% of the grains examined). Basal-type textures are observed for all compositions, but with significantly weaker basal peak intensities for Ca-containing samples when compared to pure Mg. The combination of activation of the  $\langle c + a \rangle$  slip system and texture weakening is discussed as being responsible for the improved ductility of the ternary Mg–Al–Ca alloys.

aerospace industries has generated considerable interest in the development of Mg-wrought alloys, particularly in view of the dramatic increase in the weight of electric vehicles.<sup>[2]</sup> Considering that a sport utility vehicle now weighs around 3 tonnes, lightweight materials are needed in addition to lightweight design. In particular, due to the limited room-temperature ductility of pure Mg of only 3% tensile elongation,<sup>[3]</sup> forming and machining of wrought Mg alloys is still a barrier for most applications.<sup>[4,5]</sup> The deformation of Mg and its alloys is mainly realized by basal  $\langle a \rangle$  slip and tensile twinning as the critical resolved shear stress (CRSS) of the other slip and twinning systems is significantly higher (up to 100 times).<sup>[6]</sup> This predominant activation of basal slip in conjunction with extension twinning results in the formation of basal textures during rolling.<sup>[7]</sup> Activation of non-basal slip systems, in particular  $\langle c +$

## 1. Introduction

Magnesium (Mg) and its alloys are the lightest structural materials. The use of Mg sheet material is limited due to its low room-temperature ductility, whereas cast alloys are widely used.<sup>[1]</sup> The demand for lighter materials in the automotive and


$a \rangle$  slip, can improve the room-temperature ductility by allowing strain accommodation along the crystal c-axis, that is not possible when only  $\langle a \rangle$  dislocations are active. Over the last decades, several approaches such as microstructure optimization (grain refinement<sup>[8,9]</sup> and second-phase precipitates<sup>[10]</sup>) and advanced processing (extrusion<sup>[11,12]</sup> and asymmetric forming<sup>[13]</sup>) have been pursued to improve the ductility of Mg. Further research has focused on improving the intrinsic ductility with the aim of increasing the room-temperature formability of Mg alloys. Two main strategies for increasing room-temperature ductility have been identified.<sup>[4,7,14–17]</sup> First, activation of non-basal slip systems to satisfy the von Mises criterion (i.e., activation of five independent slip systems in the single-crystal yield surface) and allow arbitrary shape changes that are not possible by basal slip alone.<sup>[4,14]</sup> Second, softening of the strong basal-type texture allows basal slip in more grains and also allows the activation of non-basal slip systems due to their higher resolved shear stresses, both of which contribute to improved formability.<sup>[7,15–17]</sup>

Previous research has shown that alloying of Mg up to a few wt% with rare-earth (RE) elements,<sup>[18–21]</sup> lithium (Li),<sup>[22–24]</sup> and yttrium (Y)<sup>[25,26]</sup> can significantly improve the intrinsic ductility. In these papers, the authors reported increased activity of non-basal slip.<sup>[18–26]</sup> However, the RE elements, Li and Y, are costly, require complex processing, and have a poor recyclability, making such alloy variants unsustainable and commercially unviable. Therefore, research on other possible alloy compositions has been investigated. Ternary alloys with Mg–Zn–Ca<sup>[27–30]</sup> have been reported to exhibit improved ductility, as have Mg–Al–Ca

W. J. Delis, P. C. Huckfeldt, P.-L. Sun, S. Korte-Kerzel, S. Sandlöbes-Haut  
Institute for Physical Metallurgy and Materials Physics  
RWTH Aachen University  
52074 Aachen, Germany  
E-mail: delis@imm.rwth-aachen.de

B. Hallstedt  
Institute for Materials Applications in Mechanical Engineering  
RWTH Aachen University  
52062 Aachen, Germany

D. Raabe  
Department of Microstructure Physics and Alloy Design  
Max-Planck Institut für Eisenforschung  
40237 Düsseldorf, Germany

 The ORCID identification number(s) for the author(s) of this article can be found under <https://doi.org/10.1002/adem.202301071>.

© 2023 The Authors. Advanced Engineering Materials published by Wiley-VCH GmbH. This is an open access article under the terms of the Creative Commons Attribution-NonCommercial-NoDerivs License, which permits use and distribution in any medium, provided the original work is properly cited, the use is non-commercial and no modifications or adaptations are made.

DOI: 10.1002/adem.202301071

alloys.<sup>[3,29,31]</sup> Solid solution Mg–Al–Ca ternary alloys have been found to give similar properties to Mg–RE, Mg–Li, and Mg–Y alloys, but the underlying dislocation slip mechanisms are still unclear.<sup>[3]</sup>

Therefore, in the present study, we investigated the activation of slip systems in binary and ternary Mg–Al–Ca with varying amounts of Al and Ca to contribute to a better understanding of the influence of Al and Ca on the texture and slip system activation. Tensile and compression testing, X-ray diffraction (XRD), electron backscatter diffraction (EBSD), and EBSD-assisted slip line analysis were used.

## 2. Experimental Section

All alloys were cast and then hot-rolled to a total thickness reduction of 50%. Casting was performed in an induction furnace under Ar atmosphere and pressure with elemental Mg, Al, and Ca (all >99.98% purity). Hot-rolling was carried out in steps of 10% thickness reduction at 430 °C with 10 min reheating in between followed by a recrystallization treatment at an annealing temperature of 450 °C for 15 min and water quenching.

An overview of the alloys studied in this work is given in **Table 1**. All compositions are in wt%, unless otherwise stated.

Thermodynamic calculations of the Mg–Al–Ca system were carried out using Thermo–Calc software<sup>[32]</sup> and the database of Janz et al.<sup>[33]</sup> This was done to investigate the solubility ranges of the alloying elements and to observe the precipitation behavior in the Mg-rich corner of the ternary-phase diagram.

Samples for mechanical testing were cut from the sheets (initial thickness between 11.9 and 13.4 mm) by electrical discharge machining. Tensile tests were performed in the transverse direction (TD) direction using flat specimens with a gauge length of 10 mm and a constant cross section of  $1.88 \times 1.50$  mm (width  $\times$  thickness). Tensile tests were performed under strain control on an electromechanical testing machine (DZM) at an initial strain rate of  $10^{-3} \text{ s}^{-1}$ . Compression test specimen had a cylindrical geometry with a height of 9 mm and a cross section of 6 mm, i.e., an aspect ratio of 1.5. Compression tests were also performed in TD using a ZWICK 1484 universal testing machine with an initial strain rate of  $10^{-3} \text{ s}^{-1}$ . A minimum of three specimens per composition and test mode were tested.

**Table 1.** Nominal compositions and chemical analysis measured by inductively coupled plasma optical emission spectrometry (ICP-OES) with impurities of the investigated compositions. All compositions are in wt%.

Sample	Nominal composition	Mg	Al	Ca	Cu	Ni
S1	1Al–0.5Ca	Bal.	1.040	0.524	<0.002	<0.002
S2	1Al–0.005Ca	Bal.	1.080	0.006	0.004	<0.002
S3	1Al–0.1Ca	Bal.	1.040	0.103	<0.002	<0.002
S4	1Al–0.2Ca	Bal.	1.100	0.232	0.002	<0.002
S5	2Al–0.005Ca	Bal.	2.110	0.007	<0.002	<0.002
S6	2Al–0.1Ca	Bal.	2.140	0.113	<0.002	<0.002
S7	2Al–0.2Ca	Bal.	2.120	0.217	0.002	<0.002
S8	0.1Ca	Bal.	0.044	0.108	<0.002	<0.002
S9	1Al	Bal.	1.000	<0.001	<0.001	<0.001

Samples for scanning electron microscopy (SEM) were first mechanically ground, then polished to 0.25  $\mu\text{m}$  with diamond paste and finally electropolished using Struers AC2 electrolyte. An SEM (Zeiss LEO1530) equipped with an EBSD detector (Oxford Instruments plc/HKL) was used for grain size measurement.

Pole figures were collected with a Bruker D8 Advanced X-ray goniometer using a  $\text{FeK}\alpha$  target. The XRD samples were mechanically ground and then polished to 3  $\mu\text{m}$  with diamond paste. Measurements were made in the normal direction (ND)–TD–plane on an area of  $6 \times 6 \mu\text{m}^2$  (S1–S8) and  $10 \times 10 \mu\text{m}^2$  (S9). For the calculation of the orientation distribution function, a value of  $3.5^\circ$  was used for both for half-width and resolution. The pole figures were then rotated to the rolling direction (RD)–TD–plane to examine the (0002)-peak intensities.

Slip line analysis was performed in the ND–TD–plane on compressed cuboidal specimens ( $1 \times 1 \text{ cm} \times$  sheet thickness), which have a flat surface parallel to the direction of loading and allow metallographic preparation for suitable slip line investigation. The preparation surface to be analyzed was identical to that used for SEM specimens. Compression was applied normal to RD until a total plastic deformation of  $\approx 3\%$  was achieved. The process was strain controlled using an initial strain rate of  $10^{-3} \text{ s}^{-1}$  on a ZWICK 1484 universal testing machine. Secondary electron (SE) images and EBSD maps for slip line analysis were obtained using a dual-beam SEM-focused ion beam (FIB) (Helios Nanolab 600i, FEI, Eindhoven, NL). For better contrast, both, the SE images and EBSD maps, were acquired under at angle of  $70^\circ$ . Tilt correction was used to transform the images and maps to  $0^\circ$  (unprojected) dimensions. The SE images were acquired at 15 kV acceleration voltage, 1.4 nA current and  $1000\times$  (S1–S8) and  $500\times$  (S9) magnification. Due to distortions, the EBSD maps were taken at  $800\times$  (S1–S8) and  $420\times$  (S9) magnification at 20 kV acceleration voltage, 5.5 nA current, and using a step size of 0.7  $\mu\text{m}$  (S1–S8) and 1  $\mu\text{m}$  (S9). The reason for using different parameters for alloy S9 is the significantly larger grain size in S9. For each alloy, three areas of the surface were analyzed and visible slip lines were correlated to the corresponding slip system.

Precipitates that formed in alloy S1 were characterized by transmission electron microscopy (TEM) on samples that were prepared site-specifically using FIB. Measurements were made using a Jeol JEM-F200 operated at 200 kV.

Data post-processing was performed using the MTEX package for MatLab,<sup>[34]</sup> and OIM Analysis 8 from EDAX and ATEX.<sup>[35]</sup>

## 3. Results

### 3.1. Thermodynamic Modeling

Prior to the experiments, Thermo–Calc was used with the database from Janz et al.<sup>[33]</sup> to calculate the solubility limits of Ca in Mg in the presence of Al. This database is widely used for Mg alloys alloyed with Al and Ca and has been shown to have a high accuracy for Mg-rich alloys, including the solubility limits of the Mg matrix. In the Mg–Al–Ca system, intermetallic Laves phases can form, of which the cubic C15  $\text{CaAl}_2$ , the hexagonal C14  $\text{CaMg}_2$ , and the hexagonal C36  $\text{Ca}(\text{Mg},\text{Al})_2$  phases have been mainly studied and can form in the Mg-rich corner.<sup>[36–40]</sup>

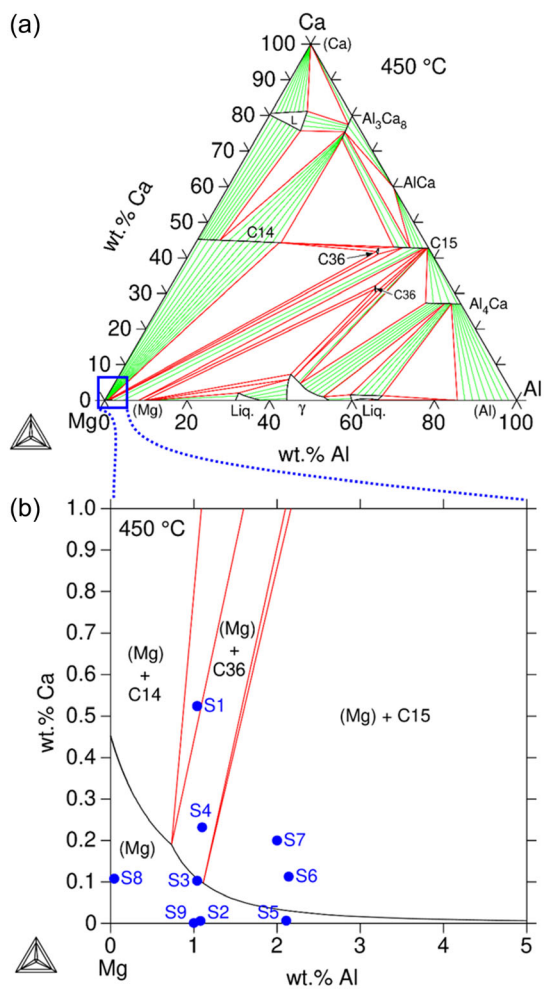


**Figure 1.** a) Calculated isothermal section of the Mg–Al–Ca system at 450 °C using Thermo–Calc and the data from Janz et al.<sup>[33]</sup> and b) the Mg-rich corner of the 450 °C isothermal section showing the compositions of the investigated alloys. S1–S9: selected alloy compositions for this study (see details in Table 1, Figure 2 and 3).

However, the stability range of the C36 phase in Mg-rich alloys is still unclear. **Figure 1** shows a) the calculated isothermal section at 450 °C and b) the Mg-rich corner including the compositions of the investigated alloys.

As can be seen in Figure 1b, the solubility of Ca decreases with increasing amount of Al. This has already been observed by Jo et al.<sup>[41]</sup> Considering the compositions studied, S2 (Mg–1Al–0.005Ca), S5 (Mg–2Al–0.005Ca), S8 (Mg–0.1Ca), and S9 (Mg–1Al) are expected to be single phase (Mg) solid solution alloys. S3 (Mg–1Al–0.1Ca) is very close to the solubility limit. S6 (Mg–2Al–0.1Ca) and S7 (Mg–2Al–0.2Ca) are above the solubility limit and could contain C15 precipitates, while S4 (Mg–1Al–0.2Ca) may contain C36 precipitates and S1 (Mg–1Al–0.5Ca) may contain both C14 and C36 precipitates. However, it should be noted that all compositions are very close to the solubility limit and, except in alloy S1 (Mg–1Al–0.5Ca), we have not observed precipitates using SEM and TEM. Alloys S4, S6, and S7 should form very few precipitates as shown in Figure 1. Ca has a strong tendency

to segregate to grain boundaries and dislocations, so that the apparent Ca solubility may be higher than the true equilibrium solubility, particularly if the grains are fine, or the dislocation density is high. It is possible that these alloys are close enough to the solubility limit not to form precipitates within the time available during annealing at 450 °C.

### 3.2. Mechanical Testing

Mechanical characterization of the alloys was carried out using tensile (**Figure 2**) and compression (**Figure 3**) tests. For clarity, only one representative tensile and compression test curve per alloy is shown in Figure 2 and 3, respectively. However, at least

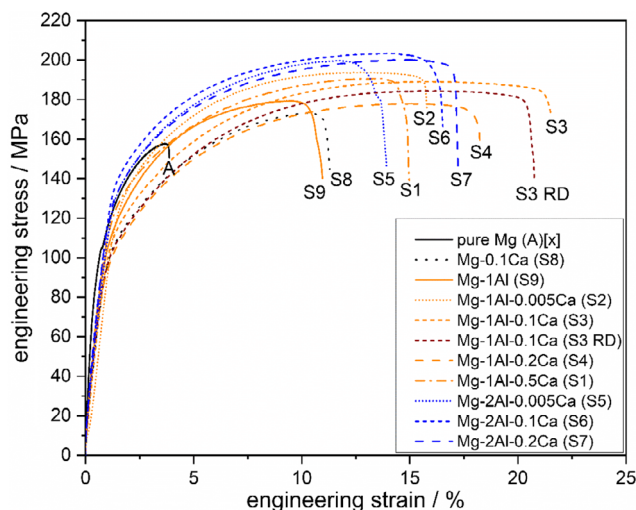


**Figure 2.** Mechanical properties obtained from tensile tests of all investigated compositions including pure Mg as reference material indicated with [X] taken from ref. [3].

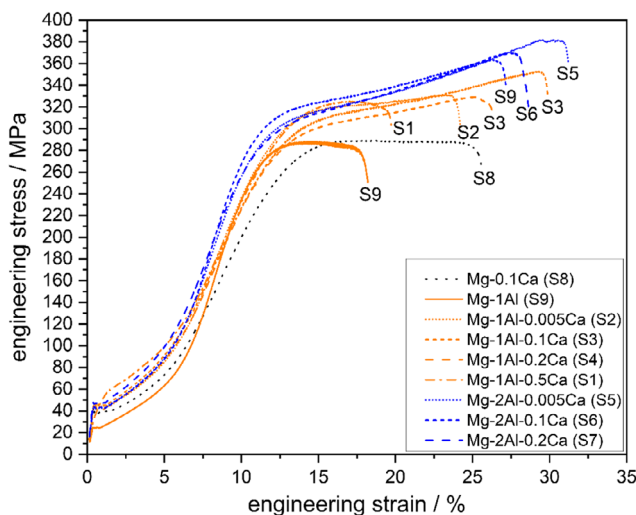


**Figure 3.** Mechanical properties obtained from compression tests of all investigated compositions.



three specimens per alloy have been tested in both tension and in compression and all show similar results. Also included is the stress–strain curve of pure Mg taken from a previous study,<sup>[3]</sup> showing very low ductility.

All the samples examined in this study, including those alloys that may contain precipitates, experience higher ductile deformation than pure Mg with tensile elongations not less than 10%. However, when comparing the binary and the ternary alloys, it is evident that the ternary alloys show significantly higher elongations than the binary alloys. Composition S3 (Mg–1Al–0.1Ca) showed the highest tensile elongations of more than 20%. The ultimate tensile strength (UTS) ranges from 172 MPa for S8 (Mg–0.1Ca) to 203 MPa for S6 (Mg–2Al–0.1Ca). As the amount of Al increases, so does the UTS. The yield strength of all alloys is approximately 87 MPa. Uniform strain and true fracture strain are close to each other for all alloys investigated. The amount of necking observed is small, resulting in a rapid loss of work hardening near the fracture point. No significant differences in the stress–strain behavior were found between RD and TD tensile specimens (evaluated as an example for S3 [Mg–1Al–0.1Ca]) (see Figure 2). Similar mechanical properties have previously been reported for a Mg–1Al–0.1Ca alloy.<sup>[3]</sup>

In addition to tensile tests, compression tests were also carried out, particularly to avoid early failure due to a relatively high level

of oxide inclusions resulting from the laboratory-scale synthesis of the alloys. The results are shown in Figure 3.

All ternary samples show an ultimate compressive strength (UCS) above 300 MPa. S5 (Mg–2Al–0.005Ca) has the highest UCS at nearly 400 MPa reaches the highest UCS. The binary compositions S8 (Mg–0.1Ca) and S9 (Mg–1Al) both have a UCS of 287 MPa, which is slightly lower than that of the ternary alloys. Furthermore, the compressive strain ranges between 15% and 28%. Binary S9 (Mg–1Al) has the lowest compressive strain. The yield strength is  $\approx$ 42 MPa for S1–S8 and 22 MPa for S9. All the compression test curves have the characteristic hump leading to an s-shaped curve, which has been reported previously in the literature.<sup>[42,43]</sup>

### 3.3. Microstructure Analysis

To study only compositional effects, synthesis and processing parameters (casting conditions, rolling degree, recrystallization temperatures, and times) were kept identical for all samples. The microstructure of all samples shows no porosity and a small (<0.5% by volume), homogeneously distributed number of oxide inclusions (see Figure 4).

The grain sizes calculated from EBSD for the samples S2–S8 are  $40 \mu\text{m} \pm 5 \mu\text{m}$  and are therefore also comparable with a

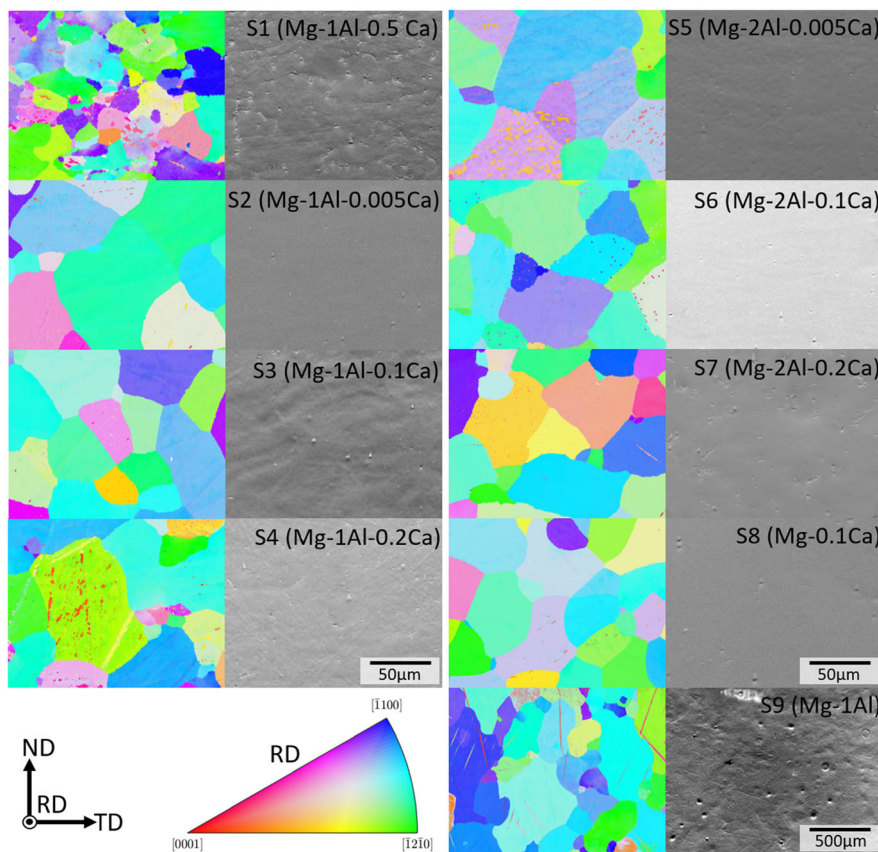


**Figure 4.** Representative electron backscatter diffraction (EBSD) map (left) and secondary electron (SE) image (right) of the normal direction–transverse direction–plane for each alloy with the corresponding inverse pole figure (IPF) color legend. The scale is identical for alloys S1–S8, but different for alloy S9 due to larger the grain size.

previous study on Mg–Al–Ca.<sup>[3]</sup> Exceptions are on the one side composition S1 (Mg–1Al–0.5Ca) with the highest Ca content, which shows reduced grain sizes of about  $17\ \mu\text{m} \pm 14\ \mu\text{m}$ , and on the other side S9 (Mg–1Al) without Ca, which shows significantly coarser grain sizes of about  $381 \pm 222\ \mu\text{m}$ . Taking this into account, we have increased the areas examined for the S9 (Mg–1Al) composition to maintain comparability in terms of the number of grains further characterized.

While alloys S2–S9 are at or very close to the solubility limit, alloy S1 contains a higher amount of Ca (0.5 wt%) and is likely to form Laves phase precipitates. Therefore, SEM,

energy-dispersive X-ray spectroscopy (EDS) and TEM were used to investigate the presence and nature of precipitates in S1 (Mg–1Al–0.5Ca). A TEM lamella was taken from the area marked by the rectangle in **Figure 5a** and subjected to EDS analysis (**Figure 5b**) and TEM diffraction (**Figure 5c**). Both methods show the presence of fine C36 Laves phase precipitates.

### 3.4. As-Recrystallized Textures

During rolling and subsequent recrystallization, Mg and most Mg alloys develop a basal texture<sup>[44,45]</sup> which affects the

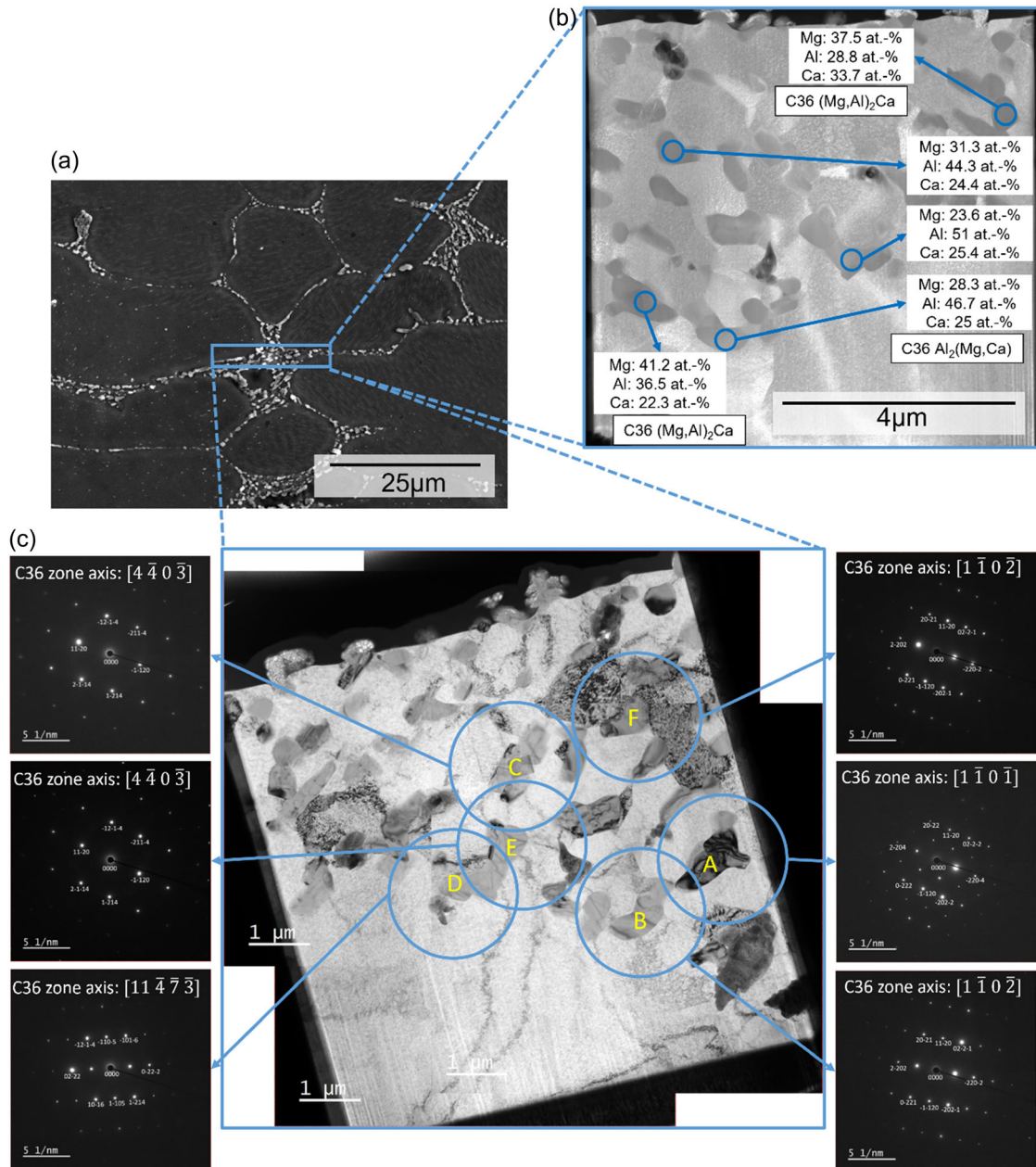


**Figure 5.** a) SE image of the S1 composition taken at 10 kV and 4.0 mm working distance (WD). Marked area for transmission electron microscopy (TEM) lamella extraction, b) scanning transmission electron microscope image taken at 30 kV and 6.0 mm WD, including energy-dispersive X-ray spectroscopy point measurements of different precipitates, and c) TEM image with diffraction patterns of selected precipitates (A–F) and zone axis showing the presence of the C36 phase.



subsequent forming processes. To investigate the relationship between texture-activated deformation mechanisms and the mechanical properties, texture measurements were carried out. **Figure 6** shows the (0002) and  $\{10\bar{1}0\}$  pole figures of the hot-rolled and recrystallized samples.

The basal texture intensities of alloys S1–S8 range from four multiples of a random distribution (m.r.d) for alloy S3 to 7.3 m.r.d for alloy S6 (Mg–2Al–0.1Ca). In contrast, alloy S9 (Mg–1Al) shows a significantly higher basal peak intensity

of 13 m.r.d. In addition, a tendency toward a TD splitting is observed.

### 3.5. Slip Line Analysis

The activation of the deformation mechanisms in alloys S1–S9 was analyzed using slip line analysis. For this purpose, several grains per alloy were examined and per grain 3–10 slip lines were analyzed. **Table 2** shows the number of grains.

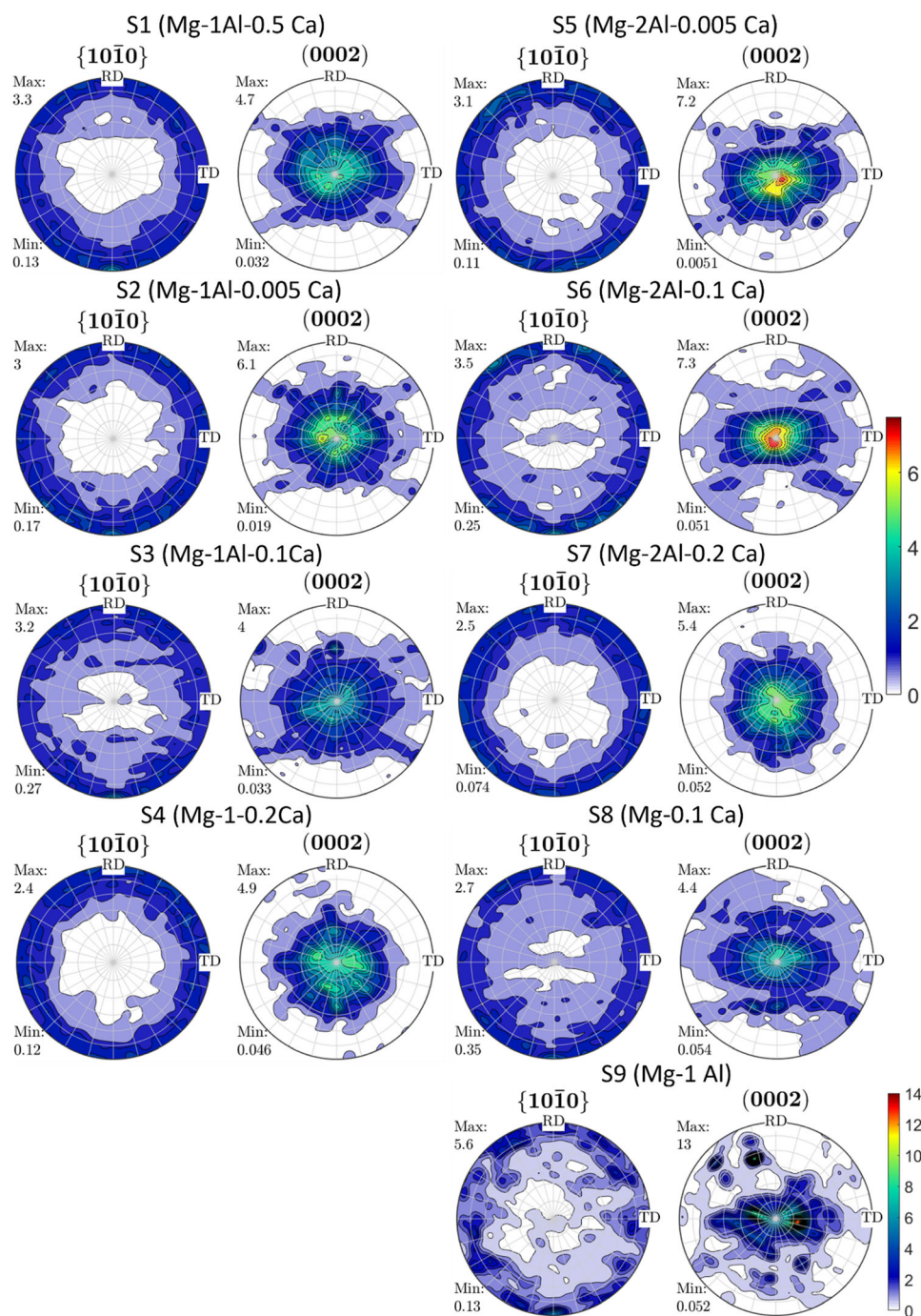


**Figure 6.** (0002) and  $\{10\bar{1}0\}$  pole figures of compositions S1–S9.

**Table 2.** Number of grains as statistical basis for the slip trace analysis.

Alloy	S1	S2	S3	S4	S5	S6	S7	S8	S9
Number of grains	68	58	41	37	51	36	54	60	57

As not all images can be shown here, we have selected a few representative images that show the observed trends of activated slip systems (Figure 7).

By correlating surface steps formed during dislocation slip on the surface with potential slip plane traces observed using EBSD, the different activated slip planes were identified (Figure 7a)). It should be noted here that  $\langle a \rangle$  dislocations can glide on basal, prismatic and first-order pyramidal planes, while  $\langle c + a \rangle$  dislocations can glide on first- and second-order pyramidal planes. Consequently, we interpret slip events on basal and prismatic planes to stem from  $\langle a \rangle$  dislocations and slip events on second-order pyramidal planes to arise due to  $\langle c + a \rangle$  dislocations (Figure 7b). For slip events on first-order pyramidal planes,  $\langle a \rangle$  and  $\langle c + a \rangle$  dislocations cannot be distinguished based on the slip plane alone. Cross-slip events between the first- and second-order planes (compare Figure 7c) can only be formed by  $\langle c + a \rangle$  dislocations.

To compare the activation of different slip planes in the alloys and to draw more general conclusions from this analysis, the relative proportion of grains showing slip on a particular slip plane is used. An overview of this analysis is given in Figure 8.

For all alloys, basal slip is the predominant active slip system that was observed in over 90% of the grains. In addition, all alloys exhibit  $\langle c + a \rangle$  second-order pyramidal slip. The binary alloy S8 (Mg–1Al) has the lowest activation frequency of second-order pyramidal slip, being observed in only 15% of the grains, while the other binary alloy S9 (Mg–1Al) has the highest amount of second-order pyramidal slip, being observed in 50% of the grains. The ternary alloys fall between these values. First-order pyramidal slip is also present in all compositions. Activation frequencies range from 18.9% to 70.2% of the grains. As mentioned earlier, both,  $\langle a \rangle$  and  $\langle c + a \rangle$  Burgers vectors, are able to slip on first-order pyramidal planes. Prismatic slip is only observed in a few grains and only in five compositions (S2 [Mg–1Al–0.005Ca], S3 [Mg–1Al–0.1Ca], S6 [Mg–2Al–0.1Ca], S8 [Mg–0.1Ca], and S9 [Mg–1Al]). Interestingly, all three alloys containing 0.1 wt% Ca show prismatic slip. It should also be noted that a high number of tensile twins were observed for all alloys but were not further analyzed in this study, as no

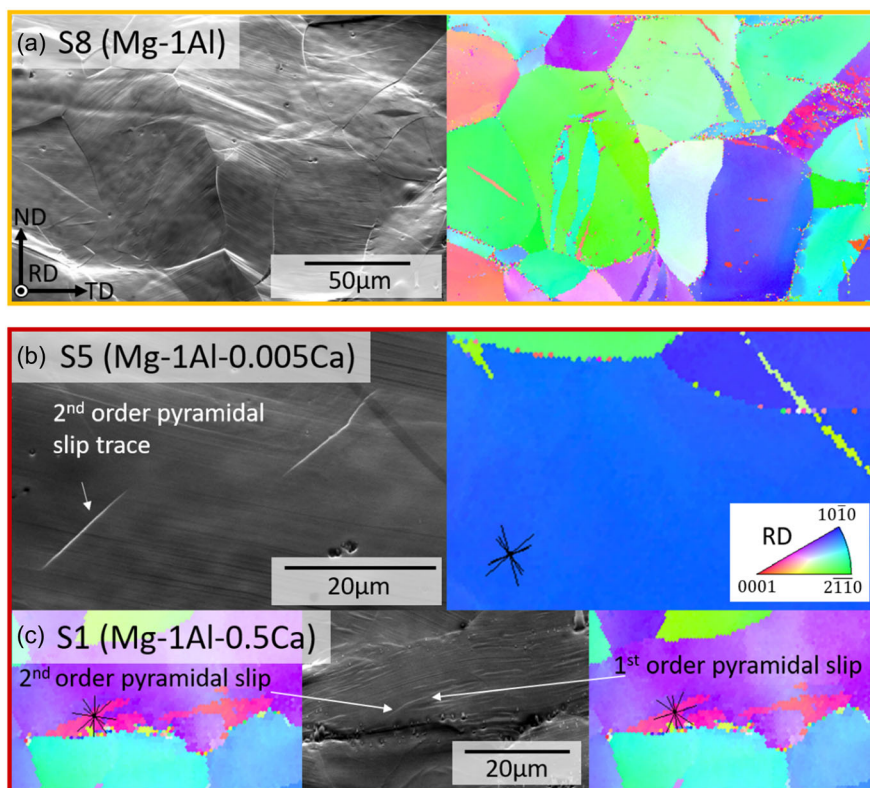


**Figure 7.** Orange box: a) example area of the correlative SE-EBSD slip line analysis of composition S8. SE image (left) and corresponding EBSD image (right) of the deformed sample. Red box: example slip lines. b) Composition S5: SE image with a second-order pyramidal slip line (left) and corresponding EBSD image with possible second-order pyramidal slip lines for the measured grain orientation (right) of the deformed sample and c) composition S1: SE image with a cross slip event between first- and second-order pyramidal slip line (center) and corresponding EBSD image with possible second-order pyramidal slip traces (left) and first-order pyramidal slip trace (right) for the measured grain orientation of the deformed sample. The sample orientation of all images and the IPF color map for EBSD images are identical for all images as indicated in (a) and (b), respectively. The total plastic deformation is  $\approx 3\%$ .



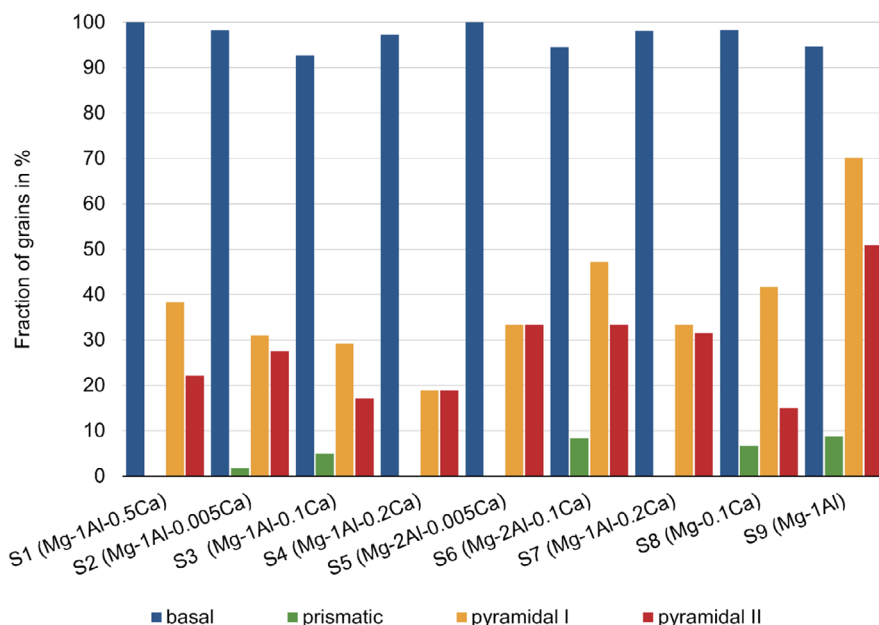


**Figure 8.** Statistical analysis of the activated slip system in each composition after a total plastic deformation of approximately 3%.

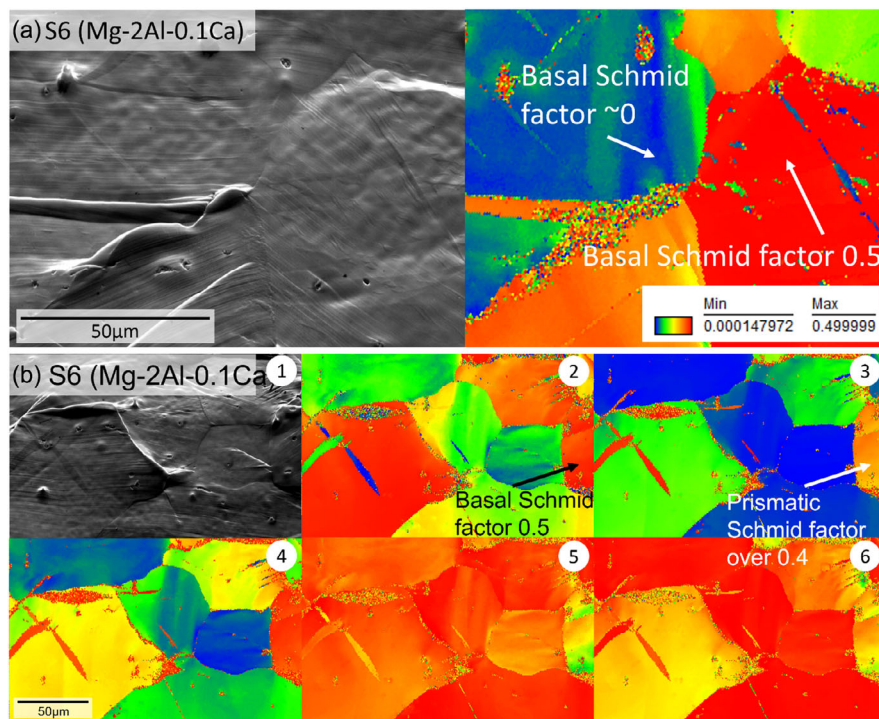


**Figure 9.** Sample S6: a) SE image with basal slip lines (left) and corresponding calculated  $m_s$  values for basal slip (right). b) 1) Overview SE image and 2) corresponding calculated  $m_s$  values for basal slip, 3) prismatic slip, 4) first-order  $\langle a \rangle$  and 5)  $\langle c + a \rangle$ , and 6) second-order pyramidal slip.

differences in the activation of tensile twinning were observed for the different alloys.

**Figure 9** shows some representative images showing the correlation between the Schmid factors and the activation of slip systems. From this analysis, it is evident that the Schmid factor for

basal slip is high in most grains due to the basal-type textures. Furthermore, as can be seen in Figure 9b (3), the Schmid factor for prismatic slip is low in most grains, presumably due to the basal-type textures. Most of the grains also have Schmid factors of  $\geq 0.4$  for first-order  $\langle c + a \rangle$  and second-order pyramidal slip



(compare Figure 9b (5) and (6)). In terms of Schmid factors for first-order pyramidal slip,  $\langle c+a \rangle$  slip has higher Schmid factors than  $\langle a \rangle$  slip (Figure 9b (4)), which is due to the more preferential geometric orientation of  $\langle c+a \rangle$  slip under compression for basal-textured Mg.<sup>[46]</sup> In most grains, the slip system with the highest Schmid factor was activated. An exception is shown in Figure 9b), where the grain was deformed by prismatic slip although the Schmid factor of prismatic slip was  $<0.4$ , which is lower than the Schmid factor for basal and first-order  $\langle a \rangle$  pyramidal slip. It should be noted that all grains with non-basal slip traces also have additional basal slip traces. If the Schmid factor for any type of pyramidal plane is less than 0.4, no slip traces belonging to that slip plane were observed.

## 4. Discussion

### 4.1. Grain Sizes

Alloys S2–S8 all show similar grain sizes of about 40  $\mu\text{m}$ . In the case of S1 (Mg–1Al–0.5Ca), the Laves phase precipitates at the grain boundaries may have resulted in reduced grain growth during recrystallization due to Zener pinning.<sup>[47]</sup> A similar effect in binary Mg–Ca alloys was recently observed by Chaudry et al.<sup>[48]</sup> Although the alloys S4 (Mg–1Al–0.2Ca), S6 (Mg–2Al–0.1Ca), and S7 (Mg–2Al–0.2Ca) have a solubility slightly above the solubility limit of Ca in a defect-free crystal, we did not observe any precipitates and expect no or only very few precipitates, which apparently do not affect the recrystallization and grain growth of the alloys. In contrast, alloy S9 (Mg–1Al), although being processed in the same way, shows much larger grains, probably due to rapid grain growth. We suggest that this is due to the absence of Ca, as it has been reported that Ca in Mg segregates to grain boundaries, improving grain-boundary strength and reducing their mobility.<sup>[49,50]</sup>

### 4.2. Mechanical Testing

As has been shown previously,<sup>[31–33]</sup> Mg–Al–Ca alloys do indeed exhibit increased intrinsic ductility relative to pure Mg and tensile elongations more than 20%. Although the alloys studied have only small variations in composition, clear differences in the deformation behavior were observed. A very small amount of Ca (0.005 wt%) already increases the ductility by  $\geq 5\%$  compared to the binary Mg–1Al sample without Ca.

In the group of alloys containing 1 wt% Al, the highest ductility under tensile loading conditions of 20.5% was obtained for the alloy containing 0.1 wt% Ca and in the group of alloys containing 2 wt% Al, the highest ductility of 17% was observed for the alloy containing 0.2 wt% Ca. This indicates that the observed ductility of ternary Mg–Al–Ca alloys may not only be an effect of the joint addition of these alloying elements, but may also be influenced by the Ca:Al ratio. Looking at the alloys investigated in the present study, the best properties are found at a Ca:Al ratio of 1:10. Previously, Sanyal et al.,<sup>[51]</sup> Li et al.,<sup>[52]</sup> and Elamami et al.<sup>[53]</sup> investigated the effects of the Ca:Al ratio of Mg–Al–Ca–Mn alloys on the solubility limits, textures, and preferred precipitate compositions and indeed showed an effect of the Ca:Al ratio on the microstructure and mechanical properties.

A similar effect was also observed by Zhang et al.<sup>[54]</sup> for ternary Mg–Al–Ca. More recently, metastable, ordered defect phases<sup>[55]</sup> have been found in Mg alloyed with Al and Ca,<sup>[56,57]</sup> and their occurrence and competition may be related to the Ca:Al ratio. The detailed characterization of these atomically ordered defects, including the deformation mechanisms and mechanical properties they give rise to, necessarily involves a large number of experiments at atomic resolution and is the subject of ongoing research.

Although the binary Mg–Ca alloy S8 (Mg–0.1Ca) has a lower ductility than the ternary alloys, the tensile and compression test results indicate that the alloying of Mg with Ca already increases the ductility when compared to pure Mg. Similar results have been reported previously by refs. [29,30]. Similarly, the binary Mg–Al alloy shows lower room-temperature ductility than the ternary alloys and the binary Mg–Ca alloy, but increased ductility compared to pure Mg. It is important to note that the compression test results consistently show higher compressive fracture strains for the binary Mg–Ca alloy than for the binary Mg–Al alloy. This may be since the compression test is less sensitive to oxide inclusions that may be present in the samples as they are produced on a laboratory scale. The increased ductility of the binary Mg–Al alloy over pure Mg is thought to be due to the lower basal texture intensity in Mg–Al than in pure Mg.

The addition of either Al (S9) or Ca (S8) results in an increase in UTS compared to pure Mg, but the ternary alloys exhibit even higher UTS values than the binary alloys. Al has been proposed to have a high-solid-solution-strengthening effect in Mg,<sup>[58,59]</sup> which agrees with our observation that increasing the Al content increases the UTS. The UTS values of alloys containing 1 and 2 wt% Al measured in the present study are comparable to those reported by Caceres et al.<sup>[58]</sup> Chino et al.<sup>[60]</sup> investigated the effects of Al and Ca on the mechanical properties of Mg and suggested that Ca has a solid-solution-softening effect in contrast to Al. Chino et al.<sup>[60]</sup> proposed that Ca causes an increased formation of double kinks for basal and prismatic slip and therefore does not act as an obstacle to dislocation movement, whereas Al acts as an obstacle for dislocation movement. The stress–strain curve of alloy S3 is in good agreement with another Mg–1Al–0.1Ca composition reported previously.<sup>[3]</sup> They<sup>[3]</sup> found that in a Mg–1Al–0.3Ca sample above the solubility limit of Ca, large and brittle C14 Mg<sub>2</sub>Ca precipitates at the grain boundaries lead to premature failure. Interestingly, the limitation of the ductility effect observed in this study does not apply to alloy S1 (Mg–1Al–0.5Ca). It is suggested, that the smaller ternary C36 precipitates observed in this study do not affect the mechanical properties as much as the large C14 precipitates. The SEM and TEM results show that these precipitates have a small platelet-shaped morphology and do not form a closed skeleton at the grain boundaries. We therefore suggest that they are less likely to initiate early cracking, as observed in the case of an interconnected C14 skeleton in a cast Mg–Al–Ca alloy.<sup>[61]</sup> The influence of the morphology of the Laves phases on the deformation behavior has also been observed by Liu et al.<sup>[62]</sup> for the interaction of deformation twinning and precipitates with different morphologies. According to the thermodynamic calculation, the observation of C36 instead of C14 is not unexpected. The observed C36 precipitates show a higher deviation from the ideal stoichiometry, including near (Mg,Al)<sub>2</sub>Ca and near Al<sub>2</sub>(Mg,Ca)

compositions, than expected from the literature. Near  $(\text{Mg,Al})_2\text{Ca}$  compositions have been measured previously by Zubair et al.,<sup>[61,63]</sup> while  $\text{Al}_2(\text{Mg,Ca})$  compositions have been reported by Zhong et al.<sup>[64]</sup> We suggest that this may be due to limited diffusion resulting in a large variation in precipitation for compositions that have not (yet) reached thermodynamic equilibrium. The actual composition and the Laves phase precipitated in Mg–Al–Ca alloys therefore depend sensitively on the processing conditions (time–temperature history).<sup>[63]</sup>

Comparing the tensile tests with the compression tests, both the UCSs and compressive strains are higher than the UTs and the tensile elongations. In contrast, the yield strengths are lower in the compression test than in tensile test. A similar tension–compression asymmetry has been observed previously and has been related with an increased activity of extension twinning due to the more favorable orientation in the compression test.<sup>[42,65–68]</sup> The asymmetry has been suggested to be 0.4–0.6, which is in good agreement with our results showing an asymmetry of about 0.5.<sup>[69]</sup> Smaller strains to failure in tension tests than in compression tests have previously been observed by other researchers.<sup>[42,66]</sup> As the difference in the strains to failure between tensile tests and compression tests for the present study is higher than expected, we assume that the higher strains achieved in compression tests are caused by oxide inclusions that cause earlier failure in tensile tests. Therefore, we assume that the tensile elongation in particular could be even higher if oxide inclusions were reduced.

Notwithstanding the higher stresses and strains observed in compression tests, the trends in alloy specific stress–strain behavior, i.e., ultimate strength, work hardening, and strain to failure, were comparable in the tension and compression tests. Minor deviations from this observation are mainly due to the scatter coming from the aforementioned oxide inclusions, because of the small laboratory scale of this study.

By separating the compressive stress–strain curves into two stages, three types of stress–strain behavior can be extracted as shown in **Figure 10**.

All alloys show a similar behavior in regime 1: a high strain hardening which occurs probably due to deformation twinning during compression.<sup>[60,64,65]</sup> In regime 2, the different alloy types show different behavior. Alloy S1 (Mg–1Al–0.5Ca) shows almost no regime 2 hardening and fails shortly after reaching the regime 2 strain hardening. The ternary alloys show steady-state strain hardening in regime 2. Similar steady-state strain hardening during compression has recently been reported in low alloy Mg–Gd alloys and the authors have proposed that this is due to the balance between strain localization and self-hardening of shear bands.<sup>[70]</sup> In addition, we assume that this is due to the interaction of different slip systems causing forest hardening and also the interaction of dislocations with twins. Deformation twinning is assumed to be less active in regime 2 strain hardening since deformation twinning in the grains, which are preferentially oriented for deformation twinning, has already twinned during regime 1 strain hardening. Finally, strain softening was observed for the binary solid solution alloys. Strain softening is usually reported for dynamic recrystallization processes at elevated temperatures<sup>[71,72]</sup> and has also been associated with the formation of double twins resulting in grains oriented more favorable for basal slip.<sup>[73,74]</sup> Indeed, we observed double twins in the

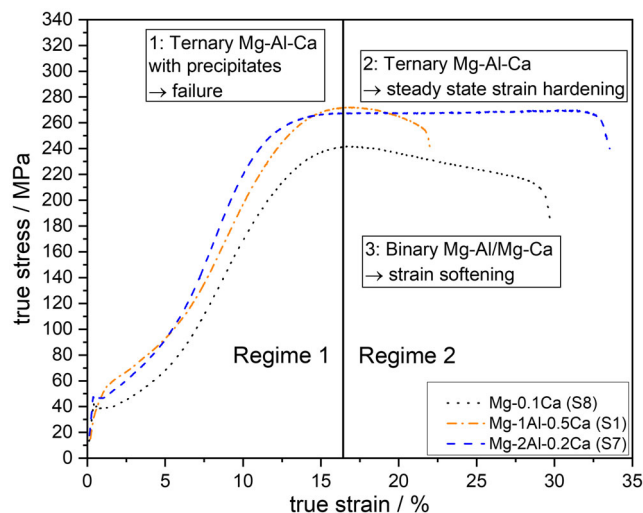


**Figure 10.** Different compressive behavior of the alloys studied represented by regime 1 and regime 2 strain hardening, exemplary for the different alloy types (ternary solid solution (S2–S7), ternary solid solution + precipitates (S1), binary solid solutions (S8 + S9)), one representative curve per group is shown.

ternary alloys at higher strains using EBSD, while no evidence of dynamic recrystallization was found. We therefore propose that the formation of double twins in the present study caused the observed strain softening.

### 4.3. Mechanisms to Improve Ductility

#### 4.3.1. Effect of Slip System Activation

One of the possible reasons for the observed increased room-temperature ductility is the activation of not only the basal but also the non-basal slip systems. Here, the activation of  $\langle c + a \rangle$  slip is the critical mechanism to satisfy the von Mises criterion and to allow the accommodation of strain along the crystal  $c$ -axis. It has been suggested that lean alloying of Al and Ca leads to enhanced activation of non-basal  $\langle c + a \rangle$  slip.<sup>[3,27,50]</sup> In general, basal slip is the dominant slip system due to the very low CRSS compared to other slip systems,<sup>[6,75]</sup> but the additional activation of  $\langle c + a \rangle$  slip can lead to increased ductility.<sup>[3,27,50]</sup> As basal dislocations produce higher surface steps and occur as parallel lines, they are easy to detect. In contrast, non-basal slip systems are less straight and form lower surface steps, making their identification is more difficult.<sup>[25]</sup> Although we carefully examined the slip traces, the detection was performed manually, and errors may occur in the correlation between the observed slip lines and the measured EBSD maps occur. Due to the distortion of the EBSD map, misalignments are possible. In case of ambiguity regarding the matching slip system, the affected slip lines were taken into account.

The slip line analysis carried out in this study showed that non-basal  $\langle c + a \rangle$  second-order pyramidal slip was indeed activated in all the compositions investigated. It should be noted that only 0.005 wt% Ca alloyed with Al is sufficient for activation. Furthermore, slip on the first-order pyramidal plane is also active

in all alloys. For most alloys, it is the predominant non-basal slip system, which has been also seen for pure Mg by Xie et al.<sup>[76]</sup> in c-axis-compressed single crystals. As both,  $\langle a \rangle$  and  $\langle c + a \rangle$  Burgers vectors can slip on the first-order pyramidal plane, we cannot conclude which of these slip systems ( $\langle a \rangle$  or  $\langle c + a \rangle$  first-order pyramidal slip) is activated without further analysis using micropillar compression and/or TEM analysis. Cross slip between the first-order pyramidal plane and the second-order pyramidal plane was observed in one grain (see Figure 7c), which has previously been discussed as a possible mechanism for  $\langle c + a \rangle$  slip.<sup>[77–79]</sup> Slip on prismatic planes has only been observed in a few compositions. Zhu et al.<sup>[80]</sup> and Chaudry et al.<sup>[81]</sup> reported that the increased ductility of Mg–Ca alloys could be based on the activation of prismatic slip, but in the present study, in addition to basal slip, slip on the pyramidal planes was mainly observed. It should also be noted that Zhu et al.<sup>[80]</sup> worked with extruded alloys, which due to the different texture, may indeed contain grains with a preferential orientation for prismatic slip. In the present study, we have investigated rolled Mg samples, which result in a basal-type texture with grain orientations that make prismatic slip difficult.

One mechanism proposed by Jang et al.<sup>[27]</sup> and Kim et al.<sup>[82]</sup> is to reduce of the CRSS anisotropy by changing the dislocation binding energy. It has been shown<sup>[27]</sup> that the ductility can be improved by adjusting the amount of Zn and Ca in Mg–Zn–Ca alloys. It has been pointed out<sup>[82]</sup> that especially the atomic size mismatch to Mg is a critical parameter for the dislocation binding energy. Considering that the atomic size of Zn is comparable to that of Al,<sup>[83]</sup> this model may also be applicable to the Mg–Al–Ca alloys studied in this work. Indeed, an increased activity of non-basal  $\langle a \rangle$  and also  $\langle c + a \rangle$  slips is observed in this study and the reduction of their CRSS and/or an increased CRSS for basal slips is a promising explanation. The interpretation of the activation of slip systems requires consideration of the resolved shear stresses on the different slip systems in a crystal. As we do not have information on the actual 3D microstructure and therefore the local stress states, we have used the Schmid factors ( $m_s$ ) as a simple approximation. It should be noted that the Schmid factors give only an approximation of the actual resolved shear stresses, as the shear induced by the neighboring grains is not included (see Figure 9). However, here we consider slip traces across many grains and will only give a relative interpretation of the slip activity on the different slip systems with different alloy contents. The increased activity of  $\langle c + a \rangle$  pyramidal slip in particular indicates that the CRSS is most likely

lower than that for pure Mg, but still significantly higher than that for basal slip. Therefore, the activation of pyramidal slip is only observed in grains with a Schmid factor  $m_s$  greater than 0.4. This result is in good agreement with calculations made by Nandy et al.<sup>[50]</sup> on similar Mg–Al–Ca alloys, showing in particular a reduction in the CRSS of non-basal slip systems; a similar effect may apply to the alloys investigated in this study.

#### 4.3.2. Effect of Texture Weakening

Weakening of the basal-type texture is a second important mechanism for the ductility of Mg and Mg alloys. Rolled Mg and Mg alloys typically develop a sharp basal-type texture which limits further deformation due to the unfavorable orientation for further deformation.<sup>[44,45,84]</sup> In weaker textures, both, basal slip and non-basal slip, can be more easily activated because the Schmid factors  $m_s$  are higher in off-basal orientations. Consequently, more grains can contribute to plastic deformation.

All the Ca-containing alloys investigated here show significantly weaker basal-type textures than pure Mg,<sup>[75,85]</sup> suggesting that i) the higher activation of non-basal slip systems results in weaker basal textures and that ii) the weaker textures may also have contributed to the increased room ductility of the alloys. Furthermore, the texture intensities show a dependence on the amount of Ca in the sample and the solubility of Ca in the alloy. **Figure 11** shows the observed influence of the Ca content and Ca solubility on the basal peak intensities.

Chapuis et al.<sup>[86]</sup> analyzed the different crystal axis rotations during deformation depending on the active slip system and the resulting lattice rotation as the sum of the rotations of all contributing slip systems, resulting in a weaker basal-type texture when non-basal slip systems are activated. A weakening of the basal texture by the addition of Ca has been reported in several studies, suggesting that the increased activation of non-basal slip may have weakened the development of a basal texture during rolling.<sup>[29,87–90]</sup> Another reason for the weakening of the basal-type texture could be a change in the recrystallization and grain growth kinetics induced by the presence of Ca atoms as proposed by Jo et al.<sup>[41]</sup> Similarly, Zeng et al.<sup>[49]</sup> suggested that the segregation of Ca at grain boundaries could influence the recrystallization behavior. The texture intensities measured in this work are in good agreement with what was suggested by Jo et al.<sup>[41]</sup> We therefore suggest that a change in recrystallization and grain growth kinetics due to the presence of Ca atoms at the grain

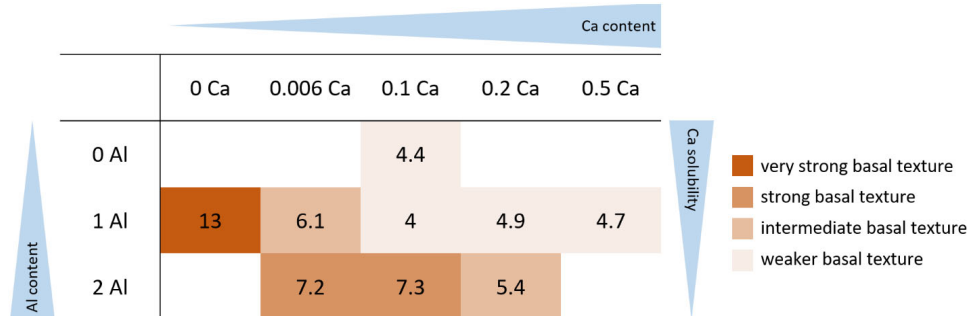


**Figure 11.** Intensities of the (0002)-peak in dependence of the Ca content and its solubility.



boundaries and the activation of non-basal slip systems causes the observed weakening of the basal texture component. This weaker basal texture then allows easier activation of both basal and non-basal dislocation slip, contributing to the observed good room-temperature ductility. It should also be noted that even 0.005 wt% Ca results in a decrease of the basal peak intensity from 13 (S9 [Mg–1Al]) to 6.1 (S2 [Mg–1Al–0.005Ca]) m.r.d., indicating that even very small amounts of Ca can affect the recrystallization and also the deformation behavior. A more comprehensive analysis of the texture-related features of this alloy system is presented in ref. [91].

## 5. Conclusions

In this study, we investigated the mechanical properties and activation of slip systems in nine Mg alloys: one binary Mg–Ca alloy, one binary Mg–Al alloy, one ternary Mg–Al–Ca alloy containing C36 precipitates, and six ternary solid solution Mg–Al–Ca alloys. It was shown that both, the activation of non-basal deformation systems and the weakened basal-type textures, lead to increased room-temperature ductility. Interestingly, only the co-addition of Ca and Al causes the observed high increase in ductility, even when the amount of Ca is very low. Although the binary alloys also show some increase in ductility, the ternary alloys show a much greater increase in ductility. The following conclusions can be drawn from the present study: 1) the co-addition of 0.005–0.5 wt% Ca and 1–2 wt% Al to Mg results in a greater increase in room-temperature ductility (10%–17%) than the addition of either Ca or Al alone (6% each). 2) The addition of Ca leads to a weakening of the basal-type texture intensity by  $\geq 6.7$  m.r.d. compared to Mg–1Al. This is thought to be due to a change in recrystallization and grain growth kinetics through the presence of Ca atoms at the grain boundaries and the activation of non-basal slip systems. Interestingly, this effect is observed even at very low levels of Ca (0.005 wt%). 3) In addition to basal slip as the dominant slip system, non-basal slip systems including  $\langle c + a \rangle$  slip were observed in 15%–33% of the grains examined for all compositions. 4) Slip on first-order and second-order pyramidal planes was observed in all compositions, while prismatic slip was preferred in compositions containing 0.1 wt% Ca. 5) Slip on pyramidal planes was only observed when the Schmid factor was greater than 0.4, indicating that the difference between the CRSS for basal slip and that for slip on pyramidal planes is still large. 6) In addition to the activation of non-basal slip systems, the weakened basal-type textures contribute to the observed ductility of the Mg–Al–Ca alloys.

## Acknowledgements

The authors gratefully acknowledge funding by the Deutsche Forschungsgemeinschaft (DFG, German Research Foundation) of SFB 1394 (CRC 1394), Project-ID 409476157, subprojects A01 und C06. The authors also thank Hauke Springer for sample synthesis, Luiz R. Guimarães for his support during samples preparation, Risheng Pei for his support during texture measurements, David Beckers for his assistance during metallographic preparation, and Gerd Schütz for sample cutting.

Open Access funding enabled and organized by Projekt DEAL.

## Conflict of Interest

The authors declare no conflict of interest.

## Data Availability Statement

The data that support the findings of this study are available from the corresponding author upon reasonable request.

## Keywords

electron microscopy, mechanical properties, Mg–Al–Ca alloys, microstructures, solid solutions

Received: July 14, 2023  
Revised: September 11, 2023  
Published online: October 15, 2023

- [1] J. F. Nie, K. S. Shin, Z. R. Zeng, *Metall. Mater. Trans. A* **2020**, *51*, 6045.
- [2] C. Romanowski, in *Magnesium Technology 2019* (Eds: V. V. Joshi, J. B. Jordon, D. Orlov, N. R. Neelameggham), Springer International Publishing, Cham **2019**, pp. 3–12.
- [3] S. Sandlöbes, M. Friák, S. Korte-Kerzel, Z. Pei, J. Neugebauer, D. Raabe, *Sci. Rep.* **2017**, *7*, 10458.
- [4] M. H. Yoo, *Metall. Mater. Trans. A* **1981**, *12*, 409.
- [5] J. Bohlen, D. Letzig, K. U. Kainer, *Mater. Sci. Forum* **2007**, *546–549*, 1.
- [6] J. Koike, T. Kobayashi, T. Mukai, H. Watanabe, M. Suzuki, K. Maruyama, K. Higashi, *Acta Mater.* **2003**, *51*, 2055.
- [7] T. Al-Samman, X. Li, *Metall. Mater. Trans. A* **2011**, *528*, 3809.
- [8] S. R. Agnew, J. A. Horton, T. M. Lillo, D. W. Brown, *Scr. Mater.* **2004**, *50*, 377.
- [9] A. Yamashita, Z. Horita, T. G. Langdon, *Metall. Mater. Trans. A* **2001**, *300*, 142.
- [10] J.-F. Nie, *Metall. Mater. Trans. A* **2012**, *43*, 3891.
- [11] T. Nakata, T. Mezaki, C. Xu, K. Oh-ishi, K. Shimizu, S. Hanaki, S. Kamado, *J. Alloys Compd.* **2015**, *648*, 428.
- [12] H. Wang, *Int. J. Plast.* **2016**, *84*, 255.
- [13] B. Beausir, S. Biswas, D. Ik Kim, L. S. Tóth, S. Suwas, *Acta Mater.* **2009**, *57*, 5061.
- [14] R. V. Mises, *Appl. Math. Mech.* **1928**, *8*, 161.
- [15] J. Bohlen, M. R. Nürnberg, J. W. Senn, D. Letzig, S. R. Agnew, *Acta Mater.* **2007**, *55*, 2101.
- [16] N. Stanford, M. Barnett, *Scr. Mater.* **2008**, *58*, 179.
- [17] L. Wang, Y. Li, H. Zhang, Z. Zhang, Q. Yang, Q. Zhang, H. Wang, W. Cheng, K. S. Shin, M. Vedani, *J. Mater. Res. Technol.* **2020**, *9*, 12604.
- [18] N. Stanford, *Metall. Mater. Trans. A* **2010**, *527*, 2669.
- [19] Y. Chino, M. Kado, M. Mabuchi, *Metall. Mater. Trans. A* **2008**, *494*, 343.
- [20] F. Wang, S. Sandlöbes, M. Diehl, L. Sharma, F. Roters, D. Raabe, *Acta Mater.* **2014**, *80*, 77.
- [21] A. Imandoust, C. D. Barrett, T. Al-Samman, K. A. Inal, H. El Kadiri, *J. Mater. Sci.* **2016**, *52*, 1.
- [22] H. Miyano, K. Takemoto, M. Tsushida, H. Kitahara, S. Ando, *Mater. Trans.* **2021**, *62*, 1097.
- [23] S. R. Agnew, J. A. Horton, M. H. Yoo, *Metall. Mater. Trans. A* **2002**, *33*, 851.
- [24] S. R. Agnew, M. H. Yoo, C. N. Tomé, *Acta Mater.* **2001**, *49*, 4277.
- [25] S. Sandlöbes, M. Friák, J. Neugebauer, D. Raabe, *Metall. Mater. Trans. A* **2013**, *576*, 61.

- [26] K. X. Sun, Y. Zeng, D. D. Yin, F. Gao, L. J. Long, X. Y. Qian, Y. J. Wan, G. F. Quan, B. Jiang, *Metall. Mater. Trans. A* **2020**, 792, 139801.
- [27] H.-S. Jang, D. Seol, B.-J. Lee, *J. Magnes. Alloy* **2021**, 9, 317.
- [28] Y. Chino, X. Huang, K. Suzuki, M. Mabuchi, *Mater. Trans.* **2010**, 51, 821.
- [29] Y. Chino, T. Ueda, Y. Otomatsu, K. Sassa, X. Huang, K. Suzuki, M. Mabuchi, *Mater. Trans.* **2011**, 52, 1477.
- [30] Z. R. Zeng, M. Z. Bian, S. W. Xu, C. H. J. Davies, N. Birbilis, J. F. Nie, *Metall. Mater. Trans. A* **2016**, 674, 459.
- [31] Q. Huang, Y. Liu, M. Tong, H. Pan, C. Yang, T. Luo, Y. Yang, *Vacuum* **2020**, 177, 109356.
- [32] J. O. Andersson, T. Helander, L. Höglund, P. Shi, B. Sundman, *Calphad* **2002**, 26, 273.
- [33] A. Janz, J. Gröbner, H. Cao, J. Zhu, Y. A. Chang, R. Schmid-Fetzer, *Acta Mater.* **2009**, 57, 682.
- [34] R. Hielscher, H. Schaeben, *J. Appl. Cryst.* **2008**, 41, 1024.
- [35] B. Beausir, J.-J. Fundenberger, ATEX - software, Université de Lorraine – Metz, **2017**, www.atex-software.eu.
- [36] A. Suzuki, N. D. Saddock, J. W. Jones, T. M. Pollock, *Acta Mater.* **2005**, 53, 2823.
- [37] M. Freund, D. Andre, C. Zehnder, H. Rempel, D. Gerber, M. Zubair, S. Sandlöbes-Haut, J. S. K.-L. Gibson, S. Korte-Kerzel, *Materialia* **2021**, 20, 101237.
- [38] H. Cao, C. Zhang, J. Zhu, G. Cao, S. Kou, R. Schmid-Fetzer, Y. A. Chang, *Acta Mater.* **2008**, 56, 5245.
- [39] W.-Y. Yu, N. Wang, X.-B. Xiao, B.-Y. Tang, L.-M. Peng, W.-J. Ding, *Solid State Sci.* **2009**, 11, 1400.
- [40] D. Kevorkov, M. Medraj, J. Li, E. Essadiqi, P. Chartrand, *Intermetallics* **2010**, 18, 1498.
- [41] S. Jo, D. Letzig, S. Yi, *Metals* **2021**, 11, 468.
- [42] X. Y. Lou, M. Li, R. K. Boger, S. R. Agnew, R. H. Wagoner, *Int. J. Plast.* **2007**, 23, 44.
- [43] E. Kelley, W. Hosford, *Trans. Met. Soc. AIME* **1968**, 242, 5.
- [44] J. Wu, L. Jin, J. Dong, F. Wang, S. Dong, *J. Mater. Sci. Technol.* **2020**, 42, 175.
- [45] Y. N. Wang, J. C. Huang, *Mater. Chem. Phys.* **2003**, 81, 11.
- [46] X.-L. Nan, H.-Y. Wang, L. Zhang, J.-B. Li, Q.-C. Jiang, *Scr. Mater.* **2012**, 67, 443.
- [47] C. S. Smith, *Trans. Metall. Soc. AIME* **1948**, 175, 15.
- [48] U. M. Chaudry, G. Han, Y. Noh, T.-S. Jun, *J. Alloys Compd.* **2023**, 950, 169828.
- [49] Z. R. Zeng, Y. M. Zhu, S. W. Xu, M. Z. Bian, C. H. J. Davies, N. Birbilis, J. F. Nie, *Acta Mater.* **2016**, 105, 479.
- [50] S. Nandy, S.-P. Tsai, L. Stephenson, D. Raabe, S. Zaeferrer, *J. Magnes. Alloy* **2021**, 9, 1521.
- [51] S. Sanyal, M. Paliwal, T. K. Bandyopadhyay, S. Mandal, *Metall. Mater. Trans. A* **2021**, 800, 140322.
- [52] Z. T. Li, X. G. Qiao, C. Xu, X. Q. Liu, S. Kamado, M. Y. Zheng, *Metall. Mater. Trans. A* **2017**, 682, 423.
- [53] H. A. Elamami, A. Incesu, K. Korgiopoulos, M. Pekguleryuz, A. Gungor, *J. Alloys Compd.* **2018**, 764, 216.
- [54] L. Zhang, K.-K. Deng, K.-B. Nie, F.-J. Xu, K. Su, W. Liang, *Metall. Mater. Trans. A* **2015**, 636, 279.
- [55] S. Korte-Kerzel, T. Hickel, L. Huber, D. Raabe, S. Sandlöbes-Haut, M. Todorova, J. Neugebauer, *Int. Mater. Rev.* **2021**, 67, 89.
- [56] A. Tehranchi, M. Lipinska-Chwalek, J. Mayer, J. Neugebauer, T. Hickel, *arXiv*, **2023**.
- [57] A. Tehranchi, S. Zhang, A. Zendegani, C. Scheu, T. Hickel, J. Neugebauer, *arXiv*, **2023**.
- [58] C. H. Cáceres, D. M. Rovera, *J. Light Met.* **2001**, 1, 151.
- [59] H. Somekawa, A. Singh, T. Mukai, T. Inoue, *Philos. Mag.* **2016**, 96, 2671.
- [60] Y. Chino, T. Ueda, M. Kado, M. Mabuchi, *Mater. Trans.* **2011**, 52, 1840.
- [61] M. Zubair, S. Sandlöbes, M. A. Wollenweber, C. F. Kusche, W. Hildebrandt, C. Broeckmann, S. Korte-Kerzel, *Metall. Mater. Trans. A* **2019**, 756, 272.
- [62] B.-Y. Liu, N. Yang, J. Wang, M. Barnett, Y.-C. Xin, D. Wu, R.-L. Xin, B. Li, R. L. Narayan, J.-F. Nie, J. Li, E. Ma, Z.-W. Shan, *J. Mater. Sci. Technol.* **2018**, 34, 1061.
- [63] M. Zubair, M. Felten, B. Hallstedt, M. V. Paredes, L. Abdellaoui, R. B. Villoro, M. Lipinska-Chwalek, N. Ayeb, H. Springer, J. Mayer, B. Berkels, D. Zander, S. Korte-Kerzel, C. Scheu, S. Zhang, *Mater. Des.* **2023**, 225, 111470.
- [64] Y. Zhong, J. Liu, R. A. Witt, Y.-h. Sohn, Z.-K. Liu, *Scr. Mater.* **2006**, 55, 573.
- [65] E. A. Ball, P. B. Prangnell, *Scr. Mater.* **1994**, 31, 111.
- [66] P. Zhou, E. Beeh, H. E. Friedrich, *J. Mater. Eng. Perform.* **2016**, 25, 853.
- [67] J. P. Nobre, U. Noster, M. Kornmeier, A. M. Dias, B. Scholtes, *Key Eng. Mater.* **2002**, 230–232, 267.
- [68] P. Klimanek, A. Pötzsch, *Metall. Mater. Trans. A* **2002**, 324, 145.
- [69] Y. Xin, X. Zhou, Q. Liu, *Metall. Mater. Trans. A* **2013**, 567, 9.
- [70] A. Kula, T. Tokarski, M. Niewczas, *Metall. Mater. Trans. A* **2020**, 51, 3742.
- [71] S. E. Ion, F. J. Humphreys, S. H. White, *Acta Metallurgica* **1982**, 30, 1909.
- [72] S. H. Choi, D. H. Kim, B. S. Seong, *Met. Mater. Int.* **2009**, 15, 239.
- [73] M. R. Barnett, in *Advances in Wrought Magnesium Alloys* (Eds: C. Bettles, M. Barnett), Woodhead Publishing, Sawston, Cambridge **2012**, pp. 105–143.
- [74] L. Jiang, J. J. Jonas, A. A. Luo, A. K. Sachdev, S. Godet, *Scr. Mater.* **2006**, 54, 771.
- [75] S. Sandlöbes, S. Zaeferrer, I. Schestakow, S. Yi, R. Gonzalez-Martinez, *Acta Mater.* **2011**, 59, 429.
- [76] K. Y. Xie, Z. Alam, A. Caffee, K. J. Hemker, *Scr. Mater.* **2016**, 112, 75.
- [77] R. Ahmad, Z. Wu, W. A. Curtin, *Acta Mater.* **2020**, 183, 228.
- [78] Z. Wu, W. A. Curtin, *Proc. Natl. Acad. Sci. U S A* **2016**, 113, 11137.
- [79] Z. Wu, R. Ahmad, B. Yin, S. Sandlöbes, W. A. Curtin, *Science* **2018**, 359, 447.
- [80] G. Zhu, L. Wang, H. Zhou, J. Wang, Y. Shen, P. Tu, H. Zhu, W. Liu, P. Jin, X. Zeng, *Int. J. Plast.* **2019**, 120, 164.
- [81] U. M. Chaudry, T. H. Kim, S. D. Park, Y. S. Kim, K. Hamad, J.-G. Kim, *Metall. Mater. Trans. A* **2019**, 739, 289.
- [82] K.-H. Kim, J. H. Hwang, H.-S. Jang, J. B. Jeon, N. J. Kim, B.-J. Lee, *Metall. Mater. Trans. A* **2018**, 715, 266.
- [83] W. Hume-Rothery, G. W. Mabbott, K. M. C. Evans, *Philos. Trans. Royal Soc. A* **1934**, 233, 1.
- [84] W. Gamin, *Textures and Plasticity*, Springer Science & Business Media, Berlin **2001**.
- [85] I. Basu, T. Al-Samman, *Metall. Mater. Trans. A* **2017**, 707, 232.
- [86] A. Chapuis, Q. Liu, *Comput. Mater. Sci.* **2015**, 97, 121.
- [87] C. Ha, J. Bohlen, S. Yi, X. Zhou, H.-G. Brokmeier, N. Schell, D. Letzig, K. U. Kainer, *Metall. Mater. Trans. A* **2019**, 761, 138053.
- [88] C. Ha, J. Bohlen, X. Zhou, H. G. Brokmeier, K. U. Kainer, N. Schell, D. Letzig, S. Yi, *Mater. Charact.* **2021**, 175, 111044.
- [89] D. Guan, X. Liu, J. Gao, L. Ma, B. P. Wynne, W. M. Rainforth, *Sci. Rep.* **2019**, 9, 7152.
- [90] J.-Y. Lee, Y.-S. Yun, W.-T. Kim, D.-H. Kim, *Met. Mater. Int.* **2014**, 20, 885.
- [91] W. J. Delis, L. Berners, S. Korte-Kerzel, S. Sandlöbes-Haut, *Metals* **2023**, 13, 712.